

FIG. 2. (Color online) Semilogarithmic plot of electrical resistivity vs temperature for  $\text{CeRu}_2\text{Al}_{10}$ . The solid line is the fit to the measured data based on the Eq. (1). Inset: a plot of  $\ln \rho$  vs  $1/T$ , showing a linear portion between 27 and 100 K, revealing a hybridization gap of 44 K.

reducing temperature,  $\rho$  increases monotonically and rises abruptly at  $T_o \sim 27$  K. It establishes a peak at  $T_p \sim 20$  K and then decreases smoothly with further cooling. The  $T$ -dependent feature is nonhysteretic in nature, which rules out the possibility of any structural phase transition. Thermally activated behavior mimicking semiconducting transport and a large magnitude of  $\rho(T) \sim 2.42$  m $\Omega$  cm at 300 K are qualitatively similar to that of the hybridized  $f$ -electron system such as  $\text{Ce}(\text{Cu}_{0.97}\text{Ni}_{0.07})\text{Si}_2$ .<sup>3</sup> The hybridization gap,  $\Delta_p = 44$  K is estimated by fitting  $\rho(T) \propto \exp(\Delta_p/2T)$  between 27 and 100 K, as shown in the inset of Fig. 2. This value is quite consistent with reported ones.<sup>1,2</sup>

We further analyze the resistivity data above  $T_o$  by using a two-band model where the dominant contribution to  $\rho(T)$  arises from the scattering of electrons within a broad  $6s$ - $5d$  conduction band and a narrow Lorentzian-shaped  $4f$  band.<sup>6</sup> The electronic density of states (DOS) of the  $4f$  band is expressed as  $N(\epsilon_F) = W/(W^2 + P^2)$ , where  $W$  and  $P$  represent the width and the position of the narrow  $f$ -electron band, respectively. The  $f$ -band position relative to  $\epsilon_F$  is given by  $P = (\epsilon_F - E_f)/k_B$ , where  $E_f$  is the energy corresponding to the center of gravity of the  $4f$  peak in the DOS. It is important to note that the parameters  $W$  and  $P$  are temperature-dependent quantities that is crucial in interpreting the low-temperature thermoelectric properties (negative minimum in Seebeck coefficient) of Kondo systems.<sup>3</sup> Thus, the total resistivity in the absence of any anomalies due to structural or electronic phase transitions is given by

$$\rho(T) = \rho_o + cT + D \frac{W}{W^2 + P^2} \quad (1)$$

with  $W = q_f \exp(-q_f/T)$  and  $P = A + B \exp(-m/T)$ , where  $A$ ,  $B$ , and  $m$  are characteristic constants for a given compound. The parameter  $q_f$  is the fluctuation temperature, providing a measure of the quasielastic linewidth governing the Abrikosov-Suhl resonance that arises from hybridization between narrow  $4f$  bands and the neighboring broad conduction bands. Constants  $\rho_o$ ,  $c$ , and  $D$  in Eq. (1) represent the residual resistivity, nonmagnetic phonon contribution, and the overlapping strength of the  $4f$  band, respectively. In this model,  $W$  is proportional to DOS in the peak that would effectively take part in the scattering process at the Fermi-level DOS,  $N(\epsilon_F)$ . Thus, within the high-temperature limit,  $W \approx q_f$ , most of the DOSs in the narrow  $f$  band are effective in the scattering. Whereas, within the low-temperature limit,  $W \ll q_f$ , only a tiny fraction of DOS contribute to the scattering process.

Figure 2 shows the nonlinear least-square fit to the experimental  $\rho(T)$  data with respect to Eq. (1). It is evident that the two-band model describes the resistivity data quite satisfactorily than simple activation-type behavior, over a wide temperature range from  $T_o$  up to 300 K. It is important to note that only  $\rho_o$ ,  $D$ , and  $q_f$  are free fitting parameters in the present analysis while the values of  $A$ ,  $B$ , and  $m$  are obtained from the analysis of the Seebeck coefficient,  $S(T)$  within the framework of this model as discussed in the following section. The magnitude of  $c$  is extracted from the slope of the  $\rho$  versus  $T$  plot within the temperature interval  $250 < T < 300$  K. We are thus able to determine the quasielastic linewidth,  $q_f = 55$  K which is self-consistent with both  $\rho(T)$  and  $S(T)$  data. These physical parameters are tabulated in Table I. It is worth noting that such analyses would be suitable for the isoelectronic  $\text{CeFe}_2\text{Al}_{10}$  and  $\text{CeOs}_2\text{Al}_{10}$  compounds.<sup>7,8</sup>

It is apparent that the experimental  $\rho(T)$  data exhibit a strong deviation from the fit near  $T_o$  as the proposed model is not valid in the vicinity of the phase transition. Below  $T_o$ , the sudden increase in  $\rho(T)$  is presumably due to the occurrence of a phase transition that opens a gap over a portion of Fermi surface as evident from low- $T$  specific-heat and Knight-shift data. The observed sharp cusp around  $T_p$  accompanied with a steep drop has been found in many Kondo systems such as  $\text{CePtSi}_2$ ,  $\text{CeRu}_2\text{Ge}_2$ , and  $\text{CeSi}_{1.3}\text{Ga}_{0.7}$ .<sup>9-11</sup>

## B. Seebeck coefficient

Seebeck coefficient and thermal conductivity measurements were simultaneously performed in a closed-cycle helium refrigerator by the direct heat pulse technique. Tempera-

TABLE I. Parameters values corresponding to the fits of the  $\rho(T)$  and  $S(T)$  data displayed in Figs. 2 and 4 based on the relations in Eqs. (1) and (2) described in the text.

$\rho_o$ ( $\mu\Omega$ cm)	$A$ (K)	$B$ (K)	$m$ (K)	$q_f$ (K)	$D$ ( $\mu\Omega$ cm K)	$c$ ( $\mu\Omega$ cm/K)	$c_1$ ( $\mu\text{V}/\text{K}^2$ )	$c_2$ ( $\mu\text{V}/\text{K}$ )
287	-0.038	186	241	55	2876	-0.23	-0.073	10.6

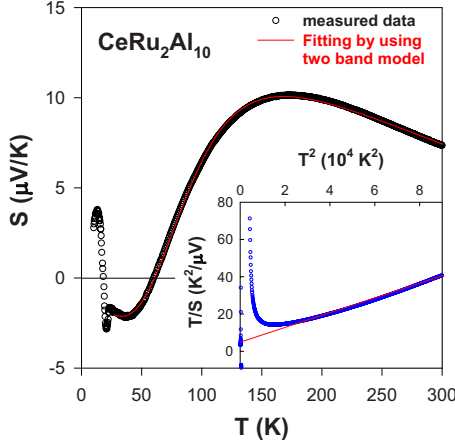


FIG. 3. (Color online) Temperature dependence of the Seebeck coefficient  $S(T)$  for  $\text{CeRu}_2\text{Al}_{10}$ . The solid line is a fit to the experimental data as described by Eq. (2). The  $T/S$  vs  $T^2$  plot is shown in the inset, indicating the validity of the two-band model. The straight line is a guide to the eyes.

ture variation in  $S(T)$  for  $\text{CeRu}_2\text{Al}_{10}$  is illustrated in Fig. 3. The striking feature in  $S(T)$  is the presence of an abrupt drop near  $T_o$ , followed by a sharp upturn accompanied by a sign change with further cooling. These phenomena are strongly related to the phase transition and the characteristic of a narrow band around the Fermi surface. Before scrutinizing the observation below  $T_o$ , we first focus our attention over the temperature range from  $T > T_o$ . The diffusion part of  $S$  in heavy-fermions and Kondo systems is completely dominant over the phonon drag contributions, leading to a broad maximum and minimum at  $\sim 100$  K and  $\sim 10$  K, respectively. This feature has been commonly found in many Ce-based compounds such as  $\text{CeCu}_2\text{Si}_2$  and  $\text{CeAl}_3$ ,<sup>12,13</sup> which has been understood within the framework of Kondo model with crystal-field excitations.<sup>14</sup>

In principle, the Seebeck coefficient is proportional to the logarithmic energy derivative of the DOS at the Fermi level. Therefore, within the framework of the two-band scenario as described in the previous section, the contribution to  $S$  from the narrow  $f$  band is expected to be proportional to  $P/(W^2 + P^2)$ , and the total measured  $S$  is given by the expression

$$S(T) = c_1 T + c_2 T \frac{P}{W^2 + P^2}, \quad (2)$$

where  $T$ -independent parameters  $c_1$  and  $c_2$  are relevant to contributions from nonmagnetic and magnetic scattering processes, respectively. As shown in the inset of Fig. 3, the linear portion of a  $T/S$  versus  $T^2$  plot from room temperature down to 40 K indicates the temperature range over which Eq. (2) is valid. It is evident from Fig. 3, where the solid line is a nonlinear-least-square fit to the experimental data using the Eq. (2), that the two-band model describes  $S(T)$  quite well over a wide temperature range. In the analysis of  $S(T)$  the value of  $A=0.038$  K is determined from the slope of the linear portion of  $S(T)$  just above  $T_o$  while the parameters  $c_1$ ,  $c_2$ ,  $B$ ,  $m$ , and  $q_f$  are used as a free fitting parameters. The parameters  $A$ ,  $B$ , and  $m$  extracted from  $S(T)$  are employed as

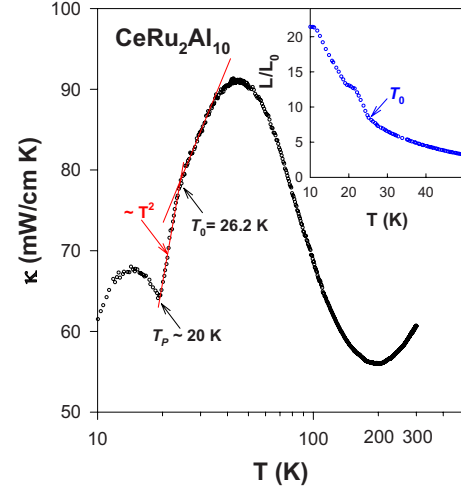


FIG. 4. (Color online) Temperature dependence of the total thermal conductivity  $\kappa(T)$  for  $\text{CeRu}_2\text{Al}_{10}$ . Inset shows the Lorentz number normalized to the Sommerfeld value as a function of temperature.

fixed parameters in the  $\rho(T)$  analysis using Eq. (1). Here  $q_f$  directly correlates with  $\rho(T)$ , and the optimum value of  $q_f$  as well as other parameters are extracted by refining both  $S(T)$  and  $\rho(T)$  iteratively. The obtained value of  $q_f=55$  K corresponding to the quasielastic linewidth  $\Gamma_{QE} \sim 4.5$  meV via the expression  $\Gamma_{QE} = k_B T$  is quite consistent with  $\Gamma_{QE} = 4 \pm 1$  meV found from the recent high-resolution inelastic neutron-scattering measurements.<sup>15</sup> The reliable values of physical parameters obtained from  $S(T)$  and  $\rho(T)$  analysis are listed in Table I.

As mentioned above,  $S(T)$  exhibits a steep fall just below  $T_o$ . This behavior is similar to that observed in  $\text{URu}_2\text{Si}_2$ , where the phase transition involves the development of unconventional SDW or the hidden-order state.<sup>16</sup> With further reducing temperature,  $S(T)$  increases sharply with a sign change from negative to positive. These observations are tentatively attributed to the dramatic change in band structure or DOS at the Fermi level, associated with the electron-hole asymmetry. Such a result would be valuable for the future band-structure calculations on  $\text{CeRu}_2\text{Al}_{10}$  and related compounds. It is noted that a recent study of the anisotropic transport properties on  $\text{CeRu}_2\text{Al}_{10}$  single crystal has indicated that  $S$  exhibits a steep increase below  $T_o$  in both  $a$  and  $c$  axes but a marked decrease in the  $b$  axis.<sup>17</sup> Our  $S(T)$  data on the polycrystalline sample can be considered as an average effect of the three crystallographic directions.

### C. Thermal conductivity

The total  $T$ -dependent thermal conductivity  $\kappa(T)$  for  $\text{CeRu}_2\text{Al}_{10}$  is shown in Fig. 4. Upon cooling,  $\kappa(T)$  decreases initially down to  $T \sim 200$  K and then develops a broad peak at around 45 K due to the reduced thermal scattering of heat-carrying phonons. With further decreasing temperature,  $\kappa(T)$  falls rapidly with a noticeable slope change near the transition temperature  $T_o \sim 27$  K and a minimum at  $T_p \sim 20$  K. Below  $T_p$ ,  $\kappa(T)$  exhibits a sudden enhancement with a peak

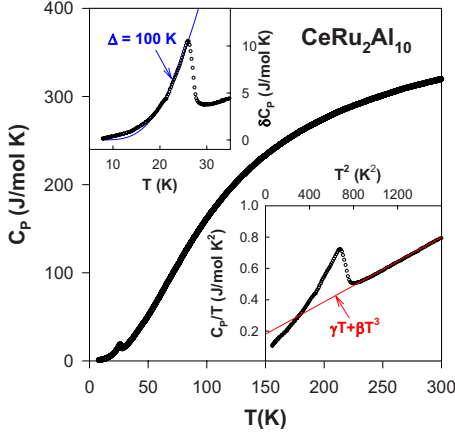


FIG. 5. (Color online) Temperature variation in the specific heat  $C_p$  for  $\text{CeRu}_2\text{Al}_{10}$ . Inset (a) shows a  $C_p/T$  vs  $T^2$  plot in the vicinity of  $T_o \sim 27$  K. A linear fit to the experimental data above  $T_o$  is used to calculate Debye temperature  $\Theta_D$  and Sommerfeld coefficient  $\gamma$ . Inset (b) displays excess specific heat,  $\delta C_p(T) \equiv C_p(T) - \gamma T - \beta T^3$  related to the phase transition as a function of temperature. The solid line is a fit to the data with an expression  $\delta C_p(T) = A \exp(-\Delta_C/T)$ .

at around 14 K. In principle, the total thermal conductivity for ordinary metals and semimetals is expressed as a sum of electronic and lattice terms. The electronic thermal conductivity ( $\kappa_e$ ) can be evaluated using the Wiedemann-Franz law  $\kappa_e \rho / T = L_o$ , where  $\rho$  is the measured dc electric resistivity and  $L_o = 2.45 \times 10^{-8} \text{ W } \Omega \text{ K}^{-2}$  is the Lorentz number. This estimate gives a very small contribution of  $\kappa_e$ , suggesting that the thermal conductivity shown in Fig. 4 is essentially due to lattice thermal conductivity ( $\kappa_L$ ). It is quite unusual that a rare-earth compound with ten Al atoms per formula unit has a negligible electronic contribution to the total thermal conductivity.

Below  $T_o$ ,  $\kappa(T)$  follows a  $T^2$  law as indicated in Fig. 4. A quadratic dependence of  $\kappa(T)$  is commonly attributed to a phononic conductivity with a predominant scattering of phonons from the charge carriers. The normalized Lorentz number  $L/L_o$ , as a function of temperature is displayed in the inset of Fig. 4. Here  $L = \kappa \rho / T$  is associated with measured  $\kappa$  and  $\rho$ . The decrease in  $L/L_o$  with respect to temperature is a consequence of the strong temperature dependence in electrical resistivity. However, the observed sudden enhancement in  $L/L_o$  near the phase transition is presumably attributed to the existence of an additional heat transport introduced by some hidden ordering. Such an unusual enhancement in  $\kappa$  below 20 K was also observed in other Kondo systems such as  $\text{URu}_2\text{Si}_2$  (Ref. 18) as well as CDW systems such as  $\text{R}_5\text{Ir}_4\text{Si}_{10}$  and  $\text{Lu}_5\text{Rh}_4\text{Si}_{10}$ .<sup>19–22</sup>

#### D. Specific heat

Specific-heat measurement was carried out with a high-resolution ac calorimeter, using chopped light as a heat source. The experimental specific heat  $C_p$  result of  $\text{CeRu}_2\text{Al}_{10}$  is given in Fig. 5. The unambiguous evidence for the presence of a phase transition is associated with a peak feature near 27 K. The shape of specific-heat jump  $\Delta C_p$  is

reminiscent of a second-order mean-field transition. As shown in the lower inset of Fig. 5, the specific heat above  $T_o$  obeys  $C_p(T) = \gamma T + \beta T^3$  with  $\gamma = 200 \text{ mJ/mol K}^2$  and  $\beta = 0.376 \text{ mJ/mol K}^4$ . Assuming that the cubic term is from phonons, we find a (per atom) Debye temperature  $\Theta_D = 407$  K. The obtained  $\gamma$  and  $\beta$  values are consistent with the earlier reported values where the measurements were performed on single crystals.<sup>2</sup> The large value of  $\gamma$  indicates that  $\text{CeRu}_2\text{Al}_{10}$  belongs to the family of heavy-fermion systems. The specific-heat jump  $\Delta C_p = 7.4 \text{ J/mol K}$  is in good agreement with the value of  $1.43 \gamma T_o = 7.72 \text{ J/mol K}$  within the mean-field theory. It thus suggests that the observed phase transition can be essentially described by a mean-field scenario. Also the measured  $\Delta C_p$  slightly less than the expected mean-field value implies that fluctuations do not have a major contribution to the specific heat.

The excess specific heat  $\delta C_p(T) \equiv C_p(T) - \gamma T - \beta T^3$  can be well described by a thermally activated form  $\delta C_p(T) = A \exp(-\Delta_C/T)$  with  $A = 400 \text{ J/mol K}$  and  $\Delta_C = 100 \text{ K} = 3.8 T_o$  (solid line in the upper inset of Fig. 5). Hence, the specific-heat data clearly reveals that the anomaly associated with the second-order phase transition involves an energy gap of about 100 K ( $\sim 8.6 \text{ meV}$ ) over a portion of Fermi surfaces which was found to be in good agreement with the Knight-shift result. It is noted that the extracted energy gap is also comparable to the value of 8 meV inferred from the recent inelastic neutron-scattering experiment and field-induced magnetic phase above 50 T in  $\text{CeRu}_2\text{Al}_{10}$ .<sup>15,23</sup>

#### E. Thermal expansion

The length change and linear thermal expansivity were measured over temperatures from 10 to 100 K using a capacitance dilatometer. The sample was cut to a rectangular parallelepiped shape of typical size of  $2 \times 2 \times 10 \text{ mm}^3$ . The dilatometer was calibrated against standard copper and aluminum samples of roughly the same length. The relative sensitivity of our dilatometer is about  $\Delta l/l \approx 10^{-10}$  for the sample of similar dimensions. Figure 6 shows the coefficient of thermal expansion  $\alpha$  for  $\text{CeRu}_2\text{Al}_{10}$  and the inset displays a closeup plot of the thermal expansivity  $\Delta l/l$  in the vicinity of the transition. A clear second-order jump in  $\alpha$  is seen at the onset of phase transition whose origin is still a mystery. It is also noted that the thermal expansion anomaly at around 27 K shares similar features as  $C_p$ , suggesting a close thermodynamic relationship for this transition. The  $T$ -dependent Gruneisen ratio in term of  $\alpha/C_p$  is illustrated in Fig. 7. As one can see, the ratio exhibits a weak temperature dependence above  $T_o$  and practically a constant above 60 K. Such an observation suggests a single energy scale and only the phonon degrees of freedom is relevant in this temperature range. An anomalous feature is also observed in the Gruneisen ratio, indicating that the electronic and magnetic contributions may come into play at the phase transition.

According to Ehrenfest relation, the specific-heat anomaly can be related to the thermal expansion for a second-order transition as

$$\Delta \alpha = \frac{1}{3V} \left( \frac{\Delta C_p}{T_o} \right) \left( \frac{dT_o}{dP} \right). \quad (3)$$

Substituting the experimental values  $\Delta \alpha = +4.2 \times 10^{-6} \text{ K}^{-1}$ ,  $\Delta C_p = 7.4 \text{ J/mol K}$ ,  $T_o = 27 \text{ K}$ , and the molar volume  $V$

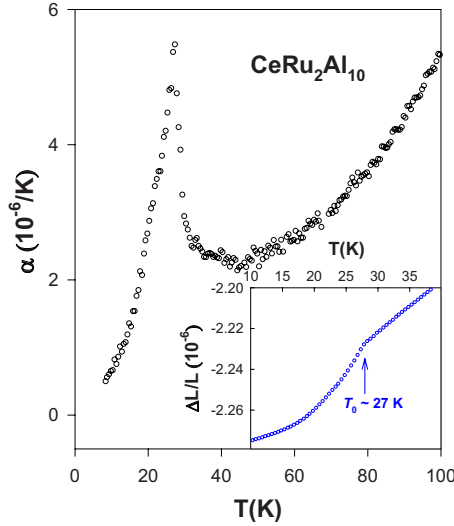


FIG. 6. (Color online) Temperature dependence of the coefficient of linear thermal expansion  $\alpha(T)$  of  $\text{CeRu}_2\text{Al}_{10}$ . Inset: a close-up  $\Delta L/L$  plot near the transition.

$=1.3 \times 10^{-4} \text{ m}^3/\text{mol}$  to Eq. (3), it yields  $dT_0/dP = +6.034 \text{ K/GPa}$  which indicates a rather large increase in  $T_0$  under hydrostatic pressure for  $\text{CeRu}_2\text{Al}_{10}$ . The calculated pressure dependence on the transition temperature is shown as the dashed line in the inset of Fig. 7 while the closed squares represent the experimental data taken by Nishioka *et al.*<sup>2</sup> It is clearly seen that our estimated  $dT_0/dP$  agrees very well with the experimental results at low pressures. However, it deviates from the linear relation with increasing pressure, presumably due to the fact that the phase transition is suppressed under high pressure.

### F. Nuclear magnetic resonance

Nuclear magnetic resonance measurements were performed using a Varian 300 spectrometer with a constant field of 6.9409 T. A home-built probe was employed for both

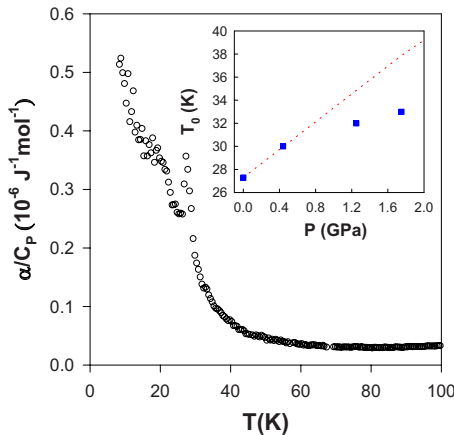


FIG. 7. (Color online) Temperature dependence of the Gruneisen ratio,  $\alpha/C_p$ , of  $\text{CeRu}_2\text{Al}_{10}$ . The inset compares the calculated pressure dependence of the transition temperature (dashed lines) with the result obtained from Ref. 1 (closed squares).

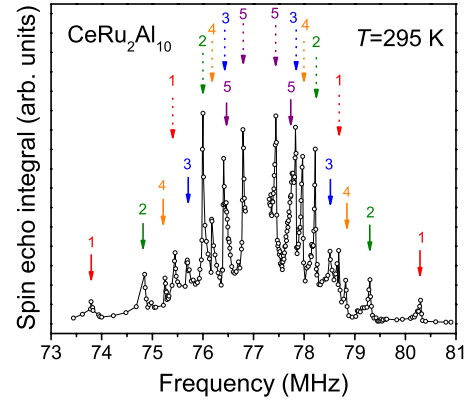


FIG. 8. (Color online) Fully resolved satellite lines for five non-equivalent crystallographic Al sites in  $\text{CeRu}_2\text{Al}_{10}$  measured at room temperature. For each individual Al site, the transitions of  $m = \pm \frac{1}{2} \leftrightarrow \pm \frac{3}{2}$  were indicated by long dashed arrows and  $m = \pm \frac{3}{2} \leftrightarrow \pm \frac{5}{2}$  by short solid arrows, respectively.

room-temperature and low-temperature experiments. To avoid the skin depth problem of the rf transmission power, a powder sample was used. The specimen was put in a plastic vial that showed no observable  $^{27}\text{Al}$  NMR signal.

In this investigation, wide-line satellite spectra were mapped out by integrating spin echo signals of various excitations. Due to electric quadrupole coupling, the  $^{27}\text{Al}$  NMR spectra ( $I = \frac{5}{2}$ ) are composed of five transition lines per site, so that five nonequivalent Al sites result in 25 resonance lines. In addition to the central transition lines which were displayed separately in Fig. 9, the remaining twenty satellite lines were resolved, as demonstrated in Fig. 8. Similar observations have been found by Matsumura *et al.*<sup>24</sup> The sharp satellite line feature in  $\text{CeRu}_2\text{Al}_{10}$  indicates that this material is well ordered, as the disorder effect usually broadens the NMR spectrum due to hyperfine-field inhomogeneity. Such a phenomenon is commonly observed in the chemically doped systems where the distinctive satellite lines gradually smear out with increasing the doping level.<sup>25,26</sup>

For a powder sample, as in our experiment, these lines exhibit a typical powder pattern with distinctive edge features corresponding to the quadrupole parameters. The four edge singularities for each Al site arise from  $m = \pm \frac{3}{2} \leftrightarrow \pm \frac{5}{2}$  (long dashed arrows) and  $m = \pm \frac{1}{2} \leftrightarrow \pm \frac{3}{2}$  (short solid arrows) transitions. Although all Al sites in  $\text{CeRu}_2\text{Al}_{10}$  are nonaxial, we found nearly even separation of the satellite lines for each individual Al site, indicating that the corresponding asymmetric parameter  $\eta \approx 0$ . It is thus valid to estimate the quadrupole frequency,  $\nu_Q$ , directly from the splitting of these lines because the first-order quadrupole interaction is the main effect shaping the satellite lines. Here  $\nu_Q = 3eQV_{zz}/[2I(2I - 1)]h$  is defined by the nuclear quadrupole moment  $Q$  and the largest principal axis component of the electric field gradient (EFG) tensor  $V_{zz}$ . This effect arises from the noncubic arrangement of the charged lattice ions and the nonuniform charge density of the conduction electrons due to orbital motion. Attempts to reproduce the observed EFG's with a simple point-charge model yield unreasonable charge transfers. In fact, the electronegativity difference between the sur-

TABLE II. Quadrupole frequency  $\nu_Q$  in MHz for each individual Al site of  $\text{CeRu}_2\text{Al}_{10}$ .

Site	Al(1)	Al(2)	Al(3)	Al(4)	Al(5)
$\nu_Q$	3.25	2.23	1.41	1.79	0.65

rounding and Al atoms is low and hence the ionicity does not play a significant role on bonding nature of  $\text{CeRu}_2\text{Al}_{10}$ . With this respect, the valance charges would be the major source for the observed EFG's.

Site identification for  $\text{CeRu}_2\text{Al}_{10}$  is given by analogy to the isostructural compound  $\text{YbFe}_2\text{Al}_{10}$  based on the site-symmetry criteria as follows.<sup>4,5,27</sup> Each Al(5) atom occupies the  $8e$  site which is the highest atomic-site symmetry among these five Al sites. Therefore Al(5) experiences the weakest EFG from the surrounding neighbors, corresponding to the smallest  $\nu_Q$  of 0.65 MHz for this site. Al(1) and Al(2) have the same site symmetry,  $8g$ , the lowest point symmetry in the present crystallographic environment. Also the averaged interatomic distance of the surrounding atoms measured from Al(1) is shorter than that from Al(2), leading to the strongest EFG sensed by the Al(1) site. It is thus reasonable to associate the largest  $\nu_Q$  of 3.25 MHz with this site. The Al(3) and the Al(4) atoms reside the  $8f$  sites, and Al(3) has a longer averaged interatomic distance than that of Al(4). By analogy to the comparison between Al(1) and Al(2), a relative small  $\nu_Q$  of 1.41 MHz should be assigned to the Al(3) site. On these bases, all observed satellite lines for  $\text{CeRu}_2\text{Al}_{10}$  were thus indexed and the corresponding  $\nu_Q$  values were summarized in Table II.

Central transition ( $m=+\frac{1}{2} \leftrightarrow -\frac{1}{2}$ ) line shapes were obtained from spin-echo fast Fourier transforms using a standard  $\pi/2$ - $\tau$ - $\pi$  sequence. Several representative spectra taken at various temperatures were showed in Fig. 9. As one can see, these spectra are quite complicated because of the combination of five Al sites and the simultaneous presence of anisotropic Knight shift as well as second-order quadrupole effects. While the latter may result in a double-peak feature for each individual Al site, the anisotropic Knight-shift effect could deform the feature, leading to a nonsymmetric single resonance line as what we observed here. Attempts to decompose each spectrum into five components using quadrupolar broadening together with the anisotropic Knight effect cannot yield an unambiguous result. On the other hand, we can resolve each Al site from quadrupole transitions as the central transition line appears approximately at the midpoint of the separated satellite lines.

At high temperatures, the spectra exhibit a clear four-line features and the high-frequency broad one was identified to be a mixture of Al(3) and Al(5) sites. The remaining three peaks from the low-frequency side were assigned to Al(1), Al(4), and Al(2), respectively. Therefore, Al(3) and Al(5) sites possess the largest Knight shift among these Al sites. Such a result is quite reasonable as both sites have two Ce atoms among the near neighbors, and thus the strongest transferred hyperfine coupling from Ce spins.<sup>4,27</sup> Below 27 K, the effect of the line splitting gradually smears out and the corresponding spectrum exhibits a two-peak feature. The low-frequency part would be the combination of Al(1),

Al(4), and Al(2) sites while the high-frequency portion should be dominated by Al(3) and Al(5) sites. Upon further cooling, all transition lines mix together, resulting in a single spectrum as observed. The whole spectrum spreads within the frequency range of about 300 kHz at 3.6 K. It is known that the width of the NMR spectrum reflects the nature of magnetic dipolar interactions, providing a direct identification for the presence of magnetic ordering.<sup>28</sup> To estimate the linewidth of each Al site, we decomposed the spectrum into five Gaussian functions, yielding an upper limit for the linewidth of  $\approx 80$  kHz at 3.6 K. This value is only about three times larger than that at a room temperature, implying an absence of a dramatic broadening in the NMR line shape below  $T_o$ . Such a result is consistent with the NQR observation and thus excludes the possibility of the SDW formation at low temperatures.<sup>24</sup>

Recently, the  $\mu^+$ SR measurement on  $\text{CeRu}_2\text{Al}_{10}$  revealed the formation of an internal field of about 30 G below  $T_o$ .<sup>29</sup> The extracted small field has been interpreted as the nonvanished magnetic moment of nearly antiparallel Ce spins. Such a result is not in contrast to the NMR observation as the extremely weak magnetic ordering has a minor effect on the line broadening. A similar result was also observed in the well-studied  $\text{URu}_2\text{Si}_2$ , which was originally found to exist a tiny staggered moment from the  $\mu$ SR measurement below

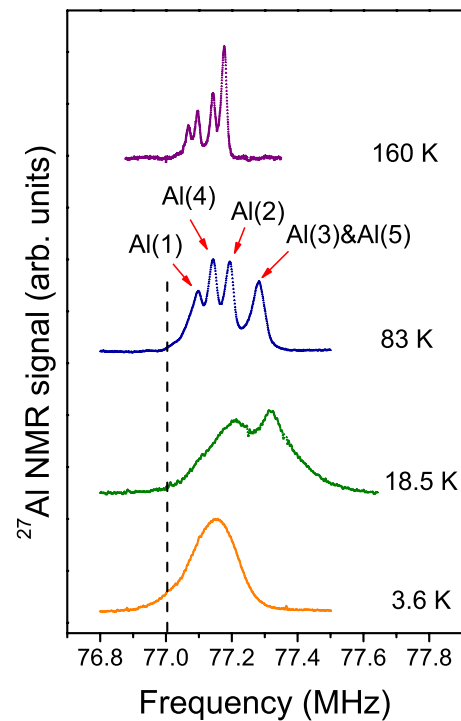


FIG. 9. (Color online)  $^{27}\text{Al}$  NMR central transition spectra of  $\text{CeRu}_2\text{Al}_{10}$  measured at various temperatures. The dashed vertical line denotes the position of the  $^{27}\text{Al}$  reference frequency.

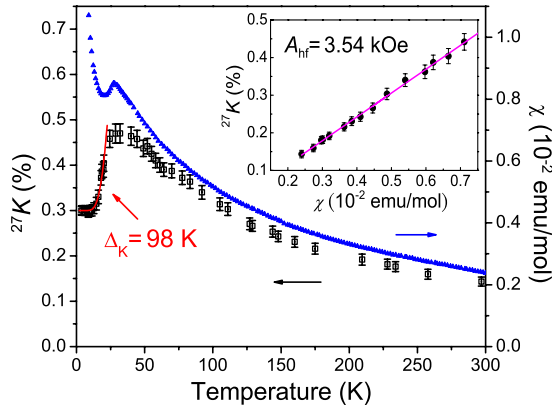


FIG. 10. (Color online) Temperature-dependent  $^{27}\text{Al}$  NMR Knight shift for the high-frequency line of  $\text{CeRu}_2\text{Al}_{10}$ . The solid curve is a fit to thermally activated behavior for  $T < T_0$ . Solid triangles represent the magnetic-susceptibility data of  $\text{CeRu}_2\text{Al}_{10}$  measured under a constant field of 1 T. The inset shows the variation in  $^{27}K$  versus  $\chi$  with a solid line indicating the linear relationship.

$T_0$ ,<sup>30</sup> but detected no evidence for the antiferromagnetic ordering from  $^{29}\text{Si}$  NMR measurement.<sup>31</sup>

The  $T$ -dependent  $^{27}\text{Al}$  NMR Knight shift ( $^{27}K$ ) for the high-frequency line of  $\text{CeRu}_2\text{Al}_{10}$  was displayed in Fig. 10. Here  $^{27}K$  was estimated from the center of the gravity of the corresponding central transition line, referred to the  $^{27}\text{Al}$  resonance frequency of one molar aqueous  $\text{AlCl}_3$ . It is apparent that the temperature variation in  $^{27}K$  is quite consistent with the magnetic susceptibility  $\chi$  above 27 K. The Knight shift here is related to the bulk magnetic susceptibility by the expression

$$^{27}K(T) = K_0 + \frac{A_{hf}}{N_A \mu_B} \chi(T), \quad (4)$$

where  $A_{hf}$  is the hyperfine coupling constant due to an intermixing of Al 3s and Ce 4f spin states. The Clogston-Jaccarino plot which shows the observed  $^{27}K$  against  $\chi$  is given in the inset of Fig. 10. The linear behavior indicates a unique hyperfine coupling constant over the high-temperature range, and the slope yields  $A_{hf} = 3.54$  kOe. It should be noted that this value is mainly associated with the transfer of Ce spins onto Al(3) and Al(5) sites in  $\text{CeRu}_2\text{Al}_{10}$ .

Below 27 K, the magnitude of  $^{27}K$  suddenly drops, following a thermally activated form:  $^{27}K(T) = K(0) + A_0 \exp(-\Delta_K/T)$ . The least-square fit gives  $\Delta_K = 98$  K, consistent with the  $\chi$  result measured on the single-crystal sample.<sup>2</sup> Here  $K(0)$  represents the  $T$ -independent Knight shift which is related to the Fermi-level DOS. We found that  $K(0) = 0.3\%$  for  $\text{CeRu}_2\text{Al}_{10}$  is larger than those of  $\text{CeFe}_2\text{Al}_{10}$ .<sup>32</sup> This comparison agrees well with the fact that  $\text{CeRu}_2\text{Al}_{10}$  possesses a large  $\gamma$  value of 200 mJ/mol K<sup>2</sup>.

To gain more insight into the low-energy spin dynamics of  $\text{CeRu}_2\text{Al}_{10}$ , we performed the spin-lattice relaxation rate ( $1/T_1$ ) measurement using the saturation recovery method. The saturation rf comb with 50 short 2  $\mu\text{s}$  pulses was employed. We recorded the decay of the signal strength by in-

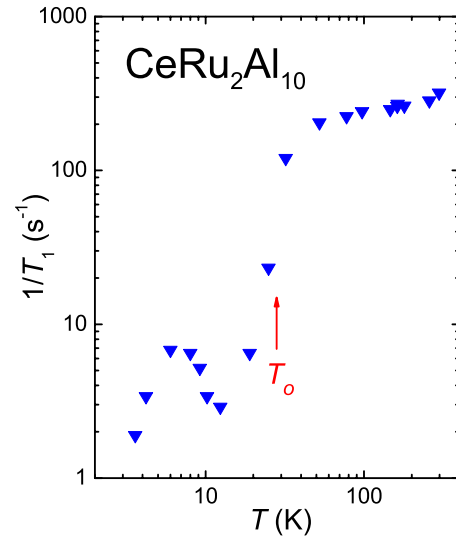


FIG. 11. (Color online) Temperature dependence of  $^{27}\text{Al}$  spin-lattice relaxation rates in  $\text{CeRu}_2\text{Al}_{10}$ .

tegrating the  $^{27}\text{Al}$  spin-echo signal. In this experiment, the relaxation process involves the adjacent pairs of spin levels, and the corresponding spin-lattice relaxation is a multiexponential expression. For the central transition with  $I = \frac{5}{2}$ , the time-dependent nuclear magnetization  $M(t)$  follows:

$$M(t) \propto (0.0286e^{-t/T_1} + 0.178e^{-6t/T_1} + 0.794e^{-15t/T_1}). \quad (5)$$

Each  $T_1$  value was thus obtained by fitting to the multiexponential function. Since it is difficult to isolate these resonance lines in the relaxation rate experiment, we only measured the high-frequency line, mainly associated with Al(2) and Al(3) sites in  $\text{CeRu}_2\text{Al}_{10}$ .

The temperature variation in  $1/T_1$  of  $\text{CeRu}_2\text{Al}_{10}$  was illustrated in Fig. 11. The entire temperature dependence of  $1/T_1$  is presumably attributed to the combination of two origins:  $1/T_1 = (1/T_1)_f + (1/T_1)_s$ . The first term represents the contribution from Ce 4f ionic magnetism while the second is the relaxation rate due to Al 3s electrons which reflects the character of the electronic DOS near the Fermi level. It is apparent that  $1/T_1$  gradually decreases with lowering temperature and exhibits a marked drop below  $T_0$ . Upon further decreasing temperature,  $1/T_1$  develops a maximum at around 7 K. The rapid reduction in  $1/T_1$  is an indication of a gaplike feature at the Fermi surfaces in spite of the additional relaxation mechanism at low temperatures. The origin of the  $1/T_1$  maximum at 7 K is not clear at this moment. Similar behavior has been observed in the Kondo lattice  $\text{SmB}_6$  which has been accounted for by the presence of a narrow band gap within highly asymmetric band edges.<sup>33</sup> Alternatively, the peak feature in  $1/T_1$  may have a magnetic origin. As a matter of fact, Tanida *et al.*<sup>34</sup> have recently investigated the magnetic field effect on the spin gap state in  $\text{CeRu}_2\text{Al}_{10}$  and observed field-induced anomalies below 10 K, which coincide with the temperature for the local minimum of  $1/T_1$ . It has been speculated that these anomalies in  $\text{CeRu}_2\text{Al}_{10}$  are intrinsic and are attributed with the fine structure in the spin

gap, possibly associated with the small internal field observed in a zero-field  $\mu^+$ SR experiment.<sup>29</sup>

The present  $1/T_1$  result clearly provides evidence for the absence of critical slowing down of the incommensurate spin dynamics toward a phase transition at  $\sim 27$  K. This finding is consistent with the NQR observation,<sup>24</sup> indicative of no SDW formation below  $T_0$ . The recent neutron-scattering measurement on  $\text{CeRu}_2\text{Al}_{10}$  also confirmed a spin-singlet state of the Ce moment.<sup>15</sup> In addition, the phase transition driven by purely electronic CDW mechanism is unlikely because the studies of La-doping effect in  $\text{Ce}_x\text{La}_{1-x}\text{Ru}_2\text{Al}_{10}$  and substantial magnetoresistance in  $\text{CeRu}_2\text{Al}_{10}$  indicated a strong association of the phase transition with the magnetic origin.<sup>35</sup> However, it is rather curious that magnetic ordering is suppressed and/or Ce moment becomes unstable in  $\text{CeRu}_2\text{Al}_{10}$ . It has been suggested that the characteristic arrangement of Ce atoms, forming dimerized Ce ion pairs along a quasi-one-dimensional direction, may be responsible for the magnetic disordered ground state.<sup>35</sup> With this respect, a simply theoretical approach based on a Ruderman-Kittel-Kasuya-Yoshida interactions along zigzag chains may induce a spin-Peierls transition in  $\text{CeRu}_2\text{Al}_{10}$ .<sup>36</sup> In any case, the true mechanism of this mysterious transition in  $\text{CeRu}_2\text{Al}_{10}$  certainly warrants further investigations.

### III. CONCLUDING REMARKS

A new heavy-fermion compound,  $\text{CeRu}_2\text{Al}_{10}$  undergoing a mean-fieldlike second-order phase transition has been es-

tablished by specific-heat and thermal-expansion measurements. Near the phase transition, all measured physical properties exhibit anomalous features and a concrete estimate of the energy gap  $\Delta \approx 100$  K was obtained from the analysis of low- $T$  specific-heat and Knight-shift data. The nonmagnetic nature of the phase transition is clearly revealed by NMR measurements. Above the transition temperature, the characteristics of both electrical transport and Seebeck coefficient can be well accounted for by a two-band model with reliable physical parameters. The extracted quasielastic linewidth  $q_f \sim 55$  K is quite consistent with the value obtained from a recent neutron-scattering measurement. In addition, we analyzed the thermal-expansion data and estimated the pressure dependence of the transition temperature, showing good agreement with the experimental result.

### ACKNOWLEDGMENTS

We are grateful to M. W. Chu and Shang Lin Hsu of the Center for Condensed Matter Sciences in National Taiwan University for the help with structural analyses. This work was supported by the National Science Council of Taiwan under Grants No. NSC-97-2628-M-259-001-MY3 (Y.K.K.) and No. NSC-98-2112-M-006-011-MY3 (C.S.L.).

\*ykkuo@mail.ndhu.edu.tw

<sup>1</sup>A. M. Strydom, *Physica B* **404**, 2981 (2009).

<sup>2</sup>T. Nishioka, Y. Kawamura, T. Takesaka, R. Kobayashi, H. Kato, M. Matsumura, K. Kodama, K. Matsubayashi, and Y. Uwatoko, *J. Phys. Soc. Jpn.* **78**, 123705 (2009).

<sup>3</sup>C. S. Garde and J. Ray, *Phys. Rev. B* **51**, 2960 (1995).

<sup>4</sup>A. I. Tursina, S. N. Nesterenko, E. V. Murashova, I. V. Chernyshev, H. Noel, and Y. D. Seropegin, *Acta Crystallogr., Sect. E: Struct. Rep. Online* **61**, i12 (2005).

<sup>5</sup>V. M. T. Thiede, T. Ebel, and W. Jeitschko, *J. Mater. Chem.* **8**, 125 (1998).

<sup>6</sup>A. Freimuth, *J. Magn. Magn. Mater.* **68**, 28 (1987).

<sup>7</sup>Y. Muro, K. Motoya, Y. Saiga, and T. Takabatake, *J. Phys. Soc. Jpn.* **78**, 083707 (2009).

<sup>8</sup>Y. Muro, J. Kajino, K. Umeo, K. Nishimoto, R. Tamura, and T. Takabatake, *Phys. Rev. B* **81**, 214401 (2010).

<sup>9</sup>T. Nakano, M. Ohashi, G. Oomi, K. Matsubayashi, and Y. Uwatoko, *Phys. Rev. B* **79**, 172507 (2009).

<sup>10</sup>H. Wilhelm, V. Zlatic, and D. Jaccard, *Physica B* **378-380**, 644 (2006).

<sup>11</sup>K. R. Priolkar, R. B. Prabhu, P. R. Sarode, V. Ganesan, P. Raj, and A. Satyamoorthy, *J. Phys.: Condens. Matter* **10**, 4413 (1998).

<sup>12</sup>D. Jaccard, J. M. Mignot, B. Bellarbi, A. Benoit, H. F. Braun, and J. Sierro, *J. Magn. Magn. Mater.* **47-48**, 23 (1995).

<sup>13</sup>N. B. Brandt and V. V. Moshchalkov, *Adv. Phys.* **33**, 373 (1984).

<sup>14</sup>K. H. Fischer, *Z. Phys. B: Condens. Matter* **76**, 315 (1989).

<sup>15</sup>J. Robert, J. Mignot, G. Andre, T. Nishioka, R. Kobayashi, M. Matsumura, H. Tanida, D. Tanaka, and M. Sera, [arXiv:1003.4933](https://arxiv.org/abs/1003.4933) (unpublished).

<sup>16</sup>R. Bel, H. Jin, K. Behnia, J. Flouquet, and P. Lejay, *Phys. Rev. B* **70**, 220501(R) (2004).

<sup>17</sup>H. Tanida, D. Tanaka, M. Sera, C. Moriyoshi, Y. Kuroiwa, T. Takesaka, T. Nishioka, H. Kato, and M. Matsumura, *J. Phys. Soc. Jpn.* **79**, 063709 (2010).

<sup>18</sup>K. Behnia, R. Bel, Y. Kasahara, Y. Nakajima, H. Jin, H. Aubin, K. Izawa, Y. Matsuda, J. Flouquet, Y. Haga, Y. Onuki, and P. Lejay, *Phys. Rev. Lett.* **94**, 156405 (2005).

<sup>19</sup>Y.-K. Kuo, C. S. Lue, F. H. Hsu, H. H. Li, and H. D. Yang, *Phys. Rev. B* **64**, 125124 (2001).

<sup>20</sup>C. S. Lue, F. H. Hsu, H. H. Li, H. D. Yang, and Y.-K. Kuo, *Physica C* **364-365**, 243 (2001).

<sup>21</sup>C. S. Lue, Y.-K. Kuo, F. H. Hsu, H. H. Li, H. D. Yang, P. S. Fodor, and L. E. Wenger, *Phys. Rev. B* **66**, 033101 (2002).

<sup>22</sup>Y.-K. Kuo, F. H. Hsu, H. H. Li, H. L. Huang, C. W. Huang, C. S. Lue, and H. D. Yang, *Phys. Rev. B* **67**, 195101 (2003).

<sup>23</sup>A. Kondo, J. Wang, K. Kindo, T. Takesaka, Y. Kawamura, T. Nishioka, D. Tanaka, H. Tanida, and M. Sera, *J. Phys. Soc. Jpn.* (to be published).

<sup>24</sup>M. Matsumura, Y. Kawamura, S. Edamoto, T. Takesaka, H. Kato, T. Nishioka, Y. Tokunagai, S. Kambe, and H. Yasuokai, *J. Phys. Soc. Jpn.* **78**, 123713 (2009).

<sup>25</sup>C. S. Lue, T. H. Su, B. X. Xie, S. K. Chen, J. L. MacManus-Driscoll, Y. K. Kuo, and H. D. Yang, *Phys. Rev. B* **73**, 214505

- (2006).
- <sup>26</sup>C. S. Lue and S. C. Chen, *Phys. Rev. B* **79**, 125108 (2009).
- <sup>27</sup>H. Noël, A. P. Gonçalves, and J. C. Waerenborgh, *Intermetallics* **12**, 189 (2004).
- <sup>28</sup>C. S. Lue, Y. Oner, D. G. Naugle, and J. H. Ross, Jr., *IEEE Trans. Magn.* **37**, 2138 (2001).
- <sup>29</sup>S. Kambe, H. Chudo, Y. Tokunaga, T. Koyama, H. Sakai, T. U. Ito, K. Ninomiya, W. Higemoto, T. Takesaka, T. Nishioka, and Y. Miyake, *J. Phys. Soc. Jpn.* **79**, 053708 (2010).
- <sup>30</sup>D. E. MacLaughlin, D. W. Cooke, R. H. Heffner, R. L. Hutson, M. W. McElfresh, M. E. Schillaci, H. D. Rempp, J. L. Smith, J. O. Willis, E. Zirngiebl, C. Boekema, R. L. Lichti, and J. Oostens, *Phys. Rev. B* **37**, 3153 (1988).
- <sup>31</sup>Y. Kohori, K. Matsuda, and T. Kohara, *J. Phys. Soc. Jpn.* **65**, 1083 (1996).
- <sup>32</sup>S. C. Chen and C. S. Lue, *Phys. Rev. B* **81**, 075113 (2010).
- <sup>33</sup>T. Caldwell, A. P. Reyes, W. G. Moulton, P. L. Kuhns, M. J. R. Hoch, P. Schlottmann, and Z. Fisk, *Phys. Rev. B* **75**, 075106 (2007).
- <sup>34</sup>H. Tanida, D. Tanaka, M. Sera, C. Moriyoshi, Y. Kuroiwa, T. Takesaka, T. Nishioka, H. Kato, and M. Matsumura, [arXiv:1005.4587](https://arxiv.org/abs/1005.4587), *J. Phys. Soc. Jpn.* (to be published).
- <sup>35</sup>H. Tanida, D. Tanaka, M. Sera, C. Moriyoshi, Y. Kuroiwa, T. Takesaka, T. Nishioka, H. Kato, and M. Matsumura, *J. Phys. Soc. Jpn.* **79**, 043708 (2010).
- <sup>36</sup>K. Hanzawa, *J. Phys. Soc. Jpn.* **79**, 043710 (2010).